Journal of Nuclear Materials 475 (2016) 156–167

Contents lists available at ScienceDirect

Journal of Nuclear Materials

journal homepage: www.elsevier.com/locate/jnucmat

Development of radiation damage during in-situ Kr^{++} irradiation of Fe–Ni–Cr model austenitic steels

M. Desormeaux [a, c, *], B. Rouxel [b], A.T. Motta [c], M. Kirk [d], C. Bisor [a], Y. de Carlan [b], A. Legris [e]

[a] DEN-Service d'Etudes des Matériaux Irradiés, CEA, Université Paris-Saclay, F-91191 Gif-sur-Yvette, France
[b] DEN-Service de Recherches Métallurgiques Appliquées, CEA, Université Paris-Saclay, F-91191 Gif-sur-Yvette, France
[c] Department of Mechanical and Nuclear Engineering, Pennsylvania State University, University Park, PA 16802, USA
[d] Electron Microscopy Center, Materials Science Division, Argonne National Laboratory, Argonne, IL 60439, USA
[e] Unité Matériaux et Transformations (UMET), UMR CNRS 8207, Université Lille 1, 59655 Villeneuve dAscq, France

ARTICLE INFO

Article history:
Received 11 October 2015
Received in revised form
7 March 2016
Accepted 7 April 2016
Available online 11 April 2016

Keywords:
In-situ
Ion-irradiation
Austenitic alloys
Dislocation loops

ABSTRACT

In situ irradiations of 15Cr/15Ni–Ti and 15Cr/25Ni–Ti model austenitic steels were performed at the Intermediate Voltage Electron Microscope (IVEM)-Tandem user Facility (Argonne National Laboratory) at 600 °C using 1 MeV Kr^{++}. The experiment was designed in the framework of cladding development for the GEN IV Sodium Fast Reactors (SFR). It is an extension of previous high dose irradiations on those model alloys at JANNuS-Saclay facility in France, aimed at investigating swelling mechanisms and microstructure evolution of these alloys under irradiation [1]. These studies showed a strong influence of Ni in decreasing swelling. In situ irradiations were used to continuously follow the microstructure evolution during irradiation using both diffraction contrast imaging and recording of diffraction patterns. Defect analysis, including defect size, density and nature, was performed to characterize the evolving microstructure and the swelling. Comparison of 15Cr/15Ni–Ti and 15Cr/25Ni–Ti irradiated microstructure has lent insight into the effect of nickel content in the development of radiation damage caused by heavy ion irradiation. The results are quantified and discussed in this paper.

1. Introduction

Austenitic stainless steels have been used as fuel cladding in fast-neutron reactors for decades. These materials offer very good required properties such as formability, weldability, compatibility with sodium, corrosion resistance and very good mechanical properties at the service temperature (400° C–700° C). Nevertheless, austenitic steels are limited by void swelling under irradiation. This phenomenon, discovered in 1967 by Refs. [2], causes dimensional changes [3,4] and embrittlement [5] of fuel assemblies which have to be replaced more frequently.

In the framework of the GEN IV Sodium Fast Reactors, the CEA (*Commissariat à l'Énergie Atomique*, French Atomic Energy Commission) has been investigating the swelling mechanism of austenitic steels in order to develop new materials, more resistant to dimensional changes, for its future Sodium Fast Reactor (SFR) ASTRID. Currently, the most optimized steel is a 15Cr/15Ni alloy (named AIM1) stabilized with titanium and used in the cold-worked condition. In order to understand the microstructural mechanisms behind the swelling phenomenon, several model alloys derived from AIM1, with different metallurgical states and chemical compositions, have been studied after ion-irradiation by [1]. Swelling under irradiation is dependent on various factors, such as the dislocation density [6–8], precipitates [7,9,10] and the chemical elements in solid solution [11–13].

Two model alloys, 15Cr/15Ni and 15Cr/25Ni, both stabilized with titanium, have been irradiated in-situ at the Intermediate Voltage Electron Microscope (IVEM)-Tandem Facility (Argonne National Laboratory) with 1Me V Kr ions. Those two model alloys had already shown different swelling behaviour after Fe^{2+}[2 Me V] ion-irradiation to 180 dpa_{KP} [1]. The objective of this work is to better understand the effect of nickel on the microstructural evolution of austenitic steels under irradiation at low doses.

* Corresponding author. DEN-Service d'Etudes des Matériaux Irradiés, CEA, Université Paris-Saclay, F-91191 Gif-sur-Yvette, France.
E-mail address: marc.desormeaux@gmail.com (M. Desormeaux).

http://dx.doi.org/10.1016/j.jnucmat.2016.04.012
0022-3115/

2. Experimental

2.1. Samples description

The experimental materials 15Cr/15Ni–Ti and 15Cr/25Ni–Ti used in this study are model alloys developed from the industrial alloy AIM1. The experimental materials, made by Rouxel [1], are shaped by rolling in a way to obtain a microstructure close to the industrial alloy AIM1 (see Fig. 1). The composition of the ingots was measured after casting by Inductively Coupled Plasma Optical Emission Spectroscopy (ICP-OES). The major constituents are given in Table 1. The main difference between those two model alloys is the higher Ni/Fe ratio in 15Cr/25Ni–Ti. Rouxel et al. have described the different stages of the fabrication process and have analyzed the final microstructure. In both model alloys, the grain size is between 20 and 60 μm, precipitates are phosphides in the matrix, (Ti,Mo)C in the matrix and at grain boundaries, and M_{23} C_6 at grain boundaries.

In order to study the effect of nickel in solid solution on the microstructure evolution during ion-irradiation, both model materials were aged at 800° C during 24 h after solution annealing. The microstructure is recrystallized and the matrix is solute-depleted. The choice of ageing conditions is based on selective dissolution experiments and time-temperature-precipitation (TTP) diagrams in order to precipitate solutes such as titanium or chromium [14,15]. Because this treatment eliminates the effect of dislocation microstructure (both alloys are similar), and the effect of solutes as well as radiation induced precipitation (because elements have been precipitated out), the specific role of the Ni-rich matrix can be more clearly separated and directly studied.

Samples are 3 mm diameter TEM foils, about 100 μm thick, electropolished to electron transparency on both faces with a solution of 5% perchloric acid and 95% methanol.

2.2. IVEM experiment

Ion irradiations were performed in a Hitachi A-9000 transmission electron microscope operating at 300 kV at the IVEM-Tandem Facility (Argonne National Laboratory). The samples were irradiated with Kr^{++} ions at 1Me V with a flux equal to 6.25×10^{15} ions m^{-2} s^{-1}.

In the IVEM facility, the ion beam is oriented 30° from the microscope axis. The specimens were tilted between 5° and 20° from the electron beam in order that they can be simultaneously irradiated by the ion beam and viewed using the electron beam. The g002 direction spot, close to [110] zone axis, was used for imaging. Both samples were observed using this same diffraction contrast.

A SRIM calculation shows that the displacement damage profile varies very little with respect to the incident angle of the ion beam when the angle is lower than 30°.

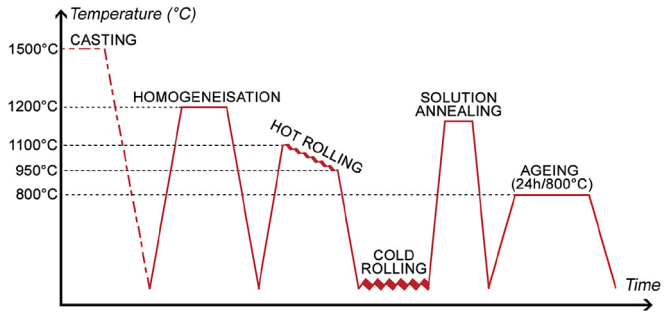

Fig. 1. Fabrication process diagram of the model alloys in this study.

Table 1
Chemical composition for major constituents of model materials as measured by ICP-OES. Units in weight percent (except for*, units in ppm).

Alloy	Fe	C*	N*	Cr	Ni	Ti	Mo
15Cr/15Ni–Ti	Bal.	950	49	14.3	16	0.42	1.5
15Cr/25Ni–Ti	Bal.	900	34	14.4	25.1	0.42	1.5

Before the experiments, the samples were heated to 600 ± 3° C by a warming resistance in the sample holder. The irradiation temperature was chosen to reach the maximum swelling conditions. The maximum peak temperature is between 525 and 550° C for austenitic steels irradiated with neutrons [16]. Since the dose rate caused by 1Me V Kr^{++} is much higher than that of fast neutrons, there is less time for thermal diffusion in between displacement events. Increasing the temperature accelerates the diffusion of point defects and allows time for microstructure evolution processes to take place, thus compensating for the higher dose rate. Accordingly, a temperature shift was calculated to allow an equivalent number of thermal jumps per dpa to occur in ion irradiation as in neutron irradiation. Following [4], the peak swelling temperature for a damage rate on the order of 10^{-3} dpa_{KP} s^{-1} is approximately 600° C, which is in accordance with experimental results [17–19].

Post irradiation characterization was performed at Penn State University using either a JEOL 2010F field emission microscope or a JEOL 2010 LaB6 microscope. Those two equipments operate at 200 kV.

2.3. Thickness measurements

In order to determine the density of defects in both samples, the thickness of the areas observed and irradiated at the IVEM were measured post-irradiation using electron energy loss spectroscopy (EELS). The EELS log ratio method and convergent beam electron diffraction (CBED) method are described in the literature [20–23]. The EELS method can be used when the sample thickness is comparable to or lower than the value of the inelastic mean free path of plasmons in the material.

The inelastic mean free path of the 15Cr/25Ni–Ti was estimated using both CBED and EELS methods on a 15Cr/25Ni–Ti non-irradiated sample. The equipment used for this experiment was a JEOL 2010F field emission microscope in STEM mode. The size of the condenser aperture, the EELS entrance aperture and the value of the camera length were chosen to yield a convergence semi-angle equal to 5.2 mrad and a collection semi-angle equal to 42.8 mrad.

The CBED measurement (see Fig. 2A) yields a thickness of 142 ± 7 nm for the non-irradiated sample at the location studied. The analysis of the electron energy loss spectrum (see Fig. 2B) recorded on the same area gives an inelastic mean free path of plasmons value equal to 110 ± 11 nm [23]. propose an empirical formula to determine the value of the inelastic mean free path, which depends on the values of the collection angle, the convergent angle and the density of the material. The calculated value of the inelastic mean free path of plasmons is 112 nm, which is very close to the experimental value.

The EELS profiles of 15Cr/15Ni–Ti and 15Cr/25Ni–Ti areas of interest (AOI) are shown in Fig. 2C and Fig. 2D, respectively. These AOI correspond to the regions observed during the irradiation experiment performed at the IVEM. The analysis of those spectra gives a thickness of 150 ± 15 nm for the 15Cr/15Ni–Ti AOI and 430 nm for the 15Cr/25Ni–Ti AOI. Although several point measurements were performed in the 15/25 area of interest and all of

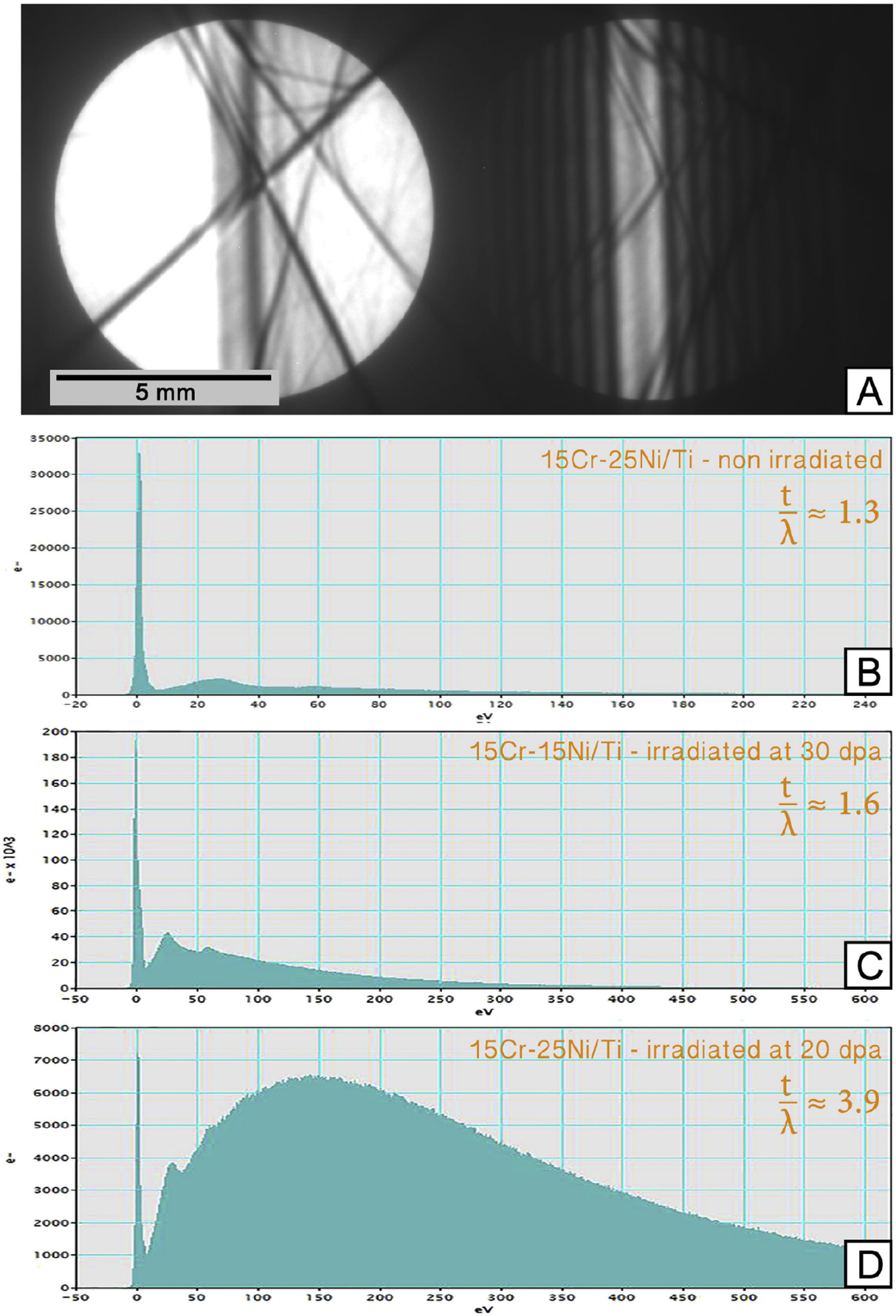

Fig. 2. (A) CBED pattern of a non-irradiated 15Cr/25Ni–Ti sample; (B) EEL spectrum of the area from where the CBED pattern was captured; (C) EEL spectrum of the 15Cr/15Ni–Ti irradiated area of interest (AOI); (D) EEL spectrum of the 15Cr/25Ni–Ti irradiated AOI.

them give a thickness close to 430 nm, this thickness value does not seem realistic. The EELS method is not reliable for the 15/25 sample because its thickness is much higher than the inelastic mean free path. The incident electrons have several interactions with the crystal and the thickness measurement is overestimated. Thus, because the contrasts observed on the micrographs are good, we consider that the thickness value for the 15Cr/25Ni–Ti sample could be between 200 and 300 nm.

2.4. Dose calculation

The damage profile of displacement per atoms (dpa) created by ion irradiation was computed for a flux of Kr^{++} at 1Me V using SRIM. The damage profile is considered to be the same for the two different alloys. The model used is the modified Kinchin and Pease quick damage estimate with the parameters recommended by [24]: displacement threshold energy equal to 40 eV and lattice and surface binding energy equal to 0 eV. The irradiation damage was calculated using the following formula:

$$dpa_{KP} = \frac{x \cdot \Phi \cdot t \cdot \mathcal{M}}{\rho \cdot \mathcal{N}_{\mathcal{A}}} \quad (1)$$

where:

- x: damage value computed with SRIM [dpa_{KP} ion^{-1} m^{-1}]
- Φ : ion flux [$ionsm^{-2}$ s^{-1}]
- t: time [s]
- $\mathcal{M}$: sample molar mass [kg mol^{-1}]
- ρ: volumetric mass [kg m^{-3}]
- $\mathcal{N}_{\mathcal{A}}$: Avogadro number [atoms mol^{-1}]

The dose rate profile is given in Fig. 3. Since the thickness of the 15/15 specimen is approximately equal to 150 nm, the average dose rate is equal to $1.2 \pm 0.2 \times 10^{-3}$ dpa_{KP} s^{-1}. In the 15/25 specimen, the AOI is thicker. The average dose rate estimated for thickness between 200 nm and 300 nm is $1.1 \pm 0.3 \times 10^{-3}$ dpa_{KP} s^{-1}.

In order to compare the size of defect depending on the irradiation dose for both materials, the dose rate chosen for both specimens is $1.2 \pm 0.2 \times 10^{-3}$ dpa_{KP} s^{-1}. Using these calculations, the 15/15 alloy was irradiated to a maximum dose of 30 dpa_{KP} and the 15/25 to 20 dpa_{KP} at a temperature of 600° C.

During irradiation, both samples were observed near the [110] zone axis using the same diffraction contrast (g002) in 2-beam conditions.

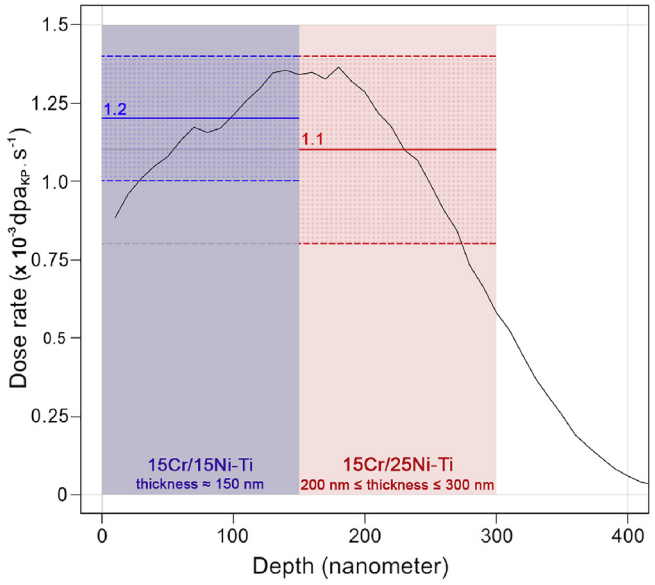

Fig. 3. Dose rate profile calculated using SRIM.

2.5. Statistical density processing

All the statistical densities were processed using the function *bkde* (package KernSmooth) of the R software [29]. Density estimation consists of a smoothing operation. There is a trade-off between bias in the estimate and the variability of the estimate: large bandwidths (equivalent to bin size) produce smooth estimates that may hide local features of the density; small bandwidths may introduce spurious bumps into the estimate. The *bkde* function gives a binned approximation to the ordinary kernel density estimate. Linear binning is used to obtain the bin counts (every 1 nm). For each diameter value where the density has to be estimated, the kernel is centered on that value and the heights of the kernel at each datapoint are summed, using a kernel bandwidth equal to 2 nm. This sum, after a normalization, is the corresponding density estimation. An example of density estimation for the 15/15 specimen at 1.08 dpa_{KP} is shown in Fig. 4.

3. Results

3.1. Development of dislocation loops

In both specimens, the main irradiation defects observed were defect clusters at low doses and dislocation loops at higher doses. The defect clusters became visible at relatively low doses (< 1 dpa_{KP}). At the beginning, small "black-dots" are visible, which are interpreted as small unresolved defect clusters. These defect clusters are frozen in the material, in contrast with the defect clusters observed in feritic alloys which were mobile under irradiation [25]. The density of "black-dots" increases with dose and they become elliptical, with a "coffee bean" contrast. As the loop diameter increases, these loops may coalesce with each other forming a dislocation network (this occurs at doses above ~1 dpa_{KP} for the 15Cr/15Ni–Ti and above ~1.6 dpa_{KP} for the 15Cr/25Ni–Ti) even while more small defect clusters become visible. Thus, it is possible to separate the loop evolution into three phases: nucleation (Fig. 5A), growth (Fig. 5B-D) and the coalescence. The coalescence of dislocation loops is shown by color arrows in Fig. 5: the two loops pointed by red arrows in Fig. 5B coalesce in one loop in Fig. 5C. This process is repeated in Fig. 5C, D and E by yellow and blue arrows. This coalescence process leads to a dense dislocation network

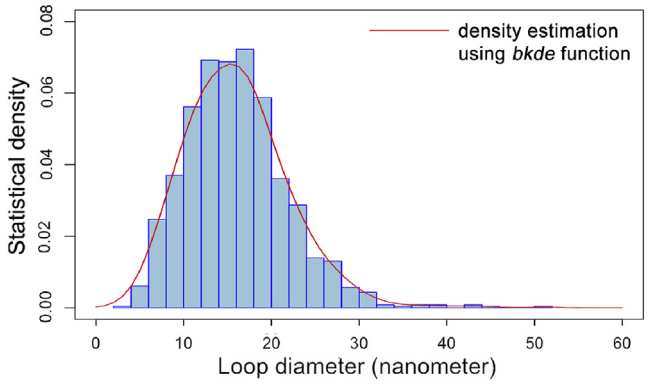

Fig. 4. Histogram of loop diameter and density estimation for the 15Cr/15Ni–Ti specimen at 1.08 dpa_{KP}. 1151 loops were measured in this case.

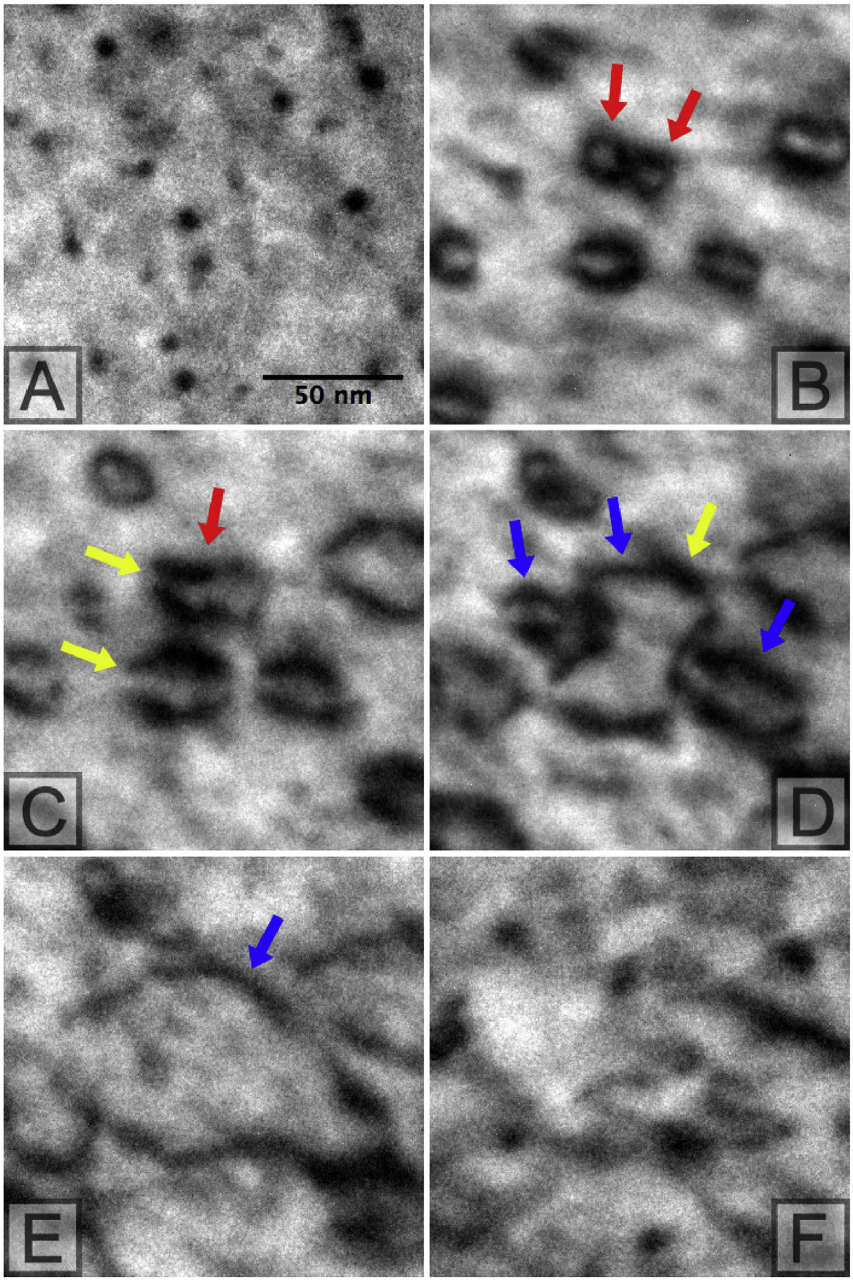

Fig. 5. Evolution of dislocation loops in the 15Cr/25Ni–Ti specimen at (A) 1.08 dpa_{KP}; (B) 1.62 dpa_{KP}; (C) 2.16 dpa_{KP}; (D) 2.71 dpa_{KP}; (E) 3.25 dpa_{KP}; (F) 4.33 dpa_{KP}.

which can absorb smaller dislocation loops (see Fig. 11D. 1 and 11.E. 1). When this step is attained, it becomes increasingly difficult to identify the dislocation loops as such.

The saturation and coalescence of dislocation loops were previously observed by [26] in neutron-irradiated austenitic steels between 5 and 10 dpa_{KP}. The size and the density of loops will be discussed in the following paragraphs. We also note that cavities were observed in thin regions of both model materials at 20 dpa_{KP} and higher doses.

3.2. Habit planes of dislocation loops

For both alloys, the same dislocation loops are observed. Dislocation loops were observed in two habit planes: {111} and {110} planes. Most loops appear elliptical, likely as a result of their habit plane being tilted with respect to the observation axis. Those loops should be circular because this shape minimizes the loop energy. Figs. 6 and 7, respectively, show the apparent shape of circular loops in the {111} and {110} planes when the foil is tilted near the [110] zone axis. Circular loops in {111} planes could be seen along three configurations and circular loops in {110} planes could be seen along four configurations.

The majority of the loops observed in both alloys (> 95%) were identified as in Fig. 8 by comparison with loop schematic as located on {111} planes. The visible loop orientations were categorized and the angle of their major axis relative to the specimen orientation were measured. As seen in Fig. 8, the angle between {111} edge-on loops and the [002] direction should be 35.26°, whereas the angles

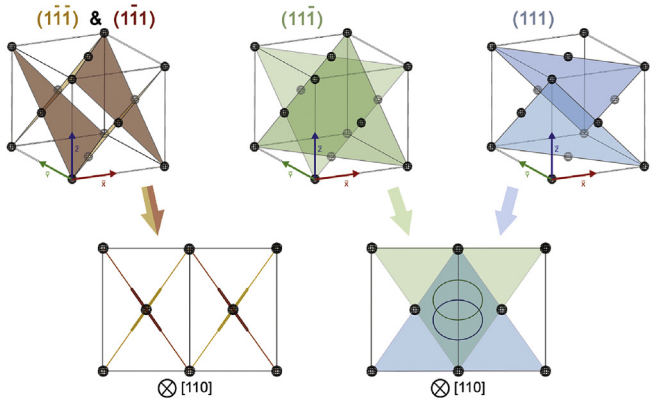

Fig. 6. {111} habit planes of dislocation loops.

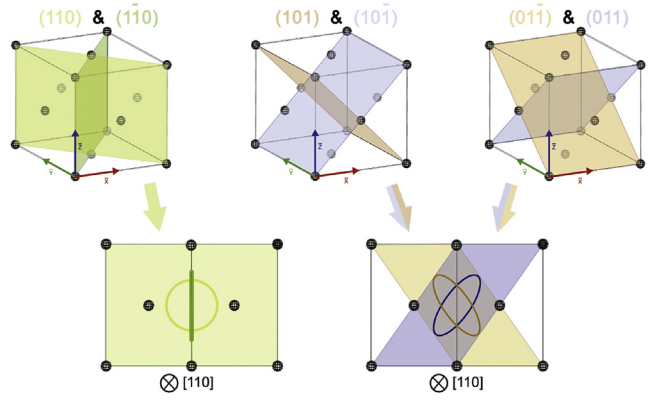

Fig. 7. {110} habit planes of dislocation loops.

measured were between 36° and 37°. Moreover, the major axis of elliptical loops is orthogonal to the diffraction vector g002 and the ratio between the major and minor axis of these loops is close to the theoretical value ($3/2 \simeq 1.22$).

As shown in Fig. 9, ({110} loop schema), some dislocation loops lie in {110} planes: elliptical loops are oriented 35° with respect to the diffraction vector [27]. has pointed out that stable interstitial or vacancy clusters and dislocation loops in f.c.c material can be either glissile in {110} planes ($\vec{b} = (1/2)\langle 110\rangle$) or sessile in {111} planes ($\vec{b} = (1/3)\langle 111\rangle$). We expect that the dislocation loops formed here have these Burgers vectors, although this was not confirmed by g.b. analysis during irradiation. This microstructure development is in agreement with previous observations in the literature which have reported the formation of faulted {111} loops which after growing and reacting with other loops, rotate to the {110} perfect loops [28,26]. The high irradiation temperature in this study may enhance the kinetics for this evolution. In this study, the majority of loops are observed in {111} planes, but it was not confirmed if they were faulted or not.

3.3. Size of dislocation loops

Even though the nature of dislocation loops appears to be similar in the two model alloys, the kinetics of formation of those defects is different. Fig. 10 shows the evolution of two areas in the 15Cr/15Ni–Ti and 15Cr/25Ni–Ti specimens at five different doses. It is clear that the nucleation of loops appears much earlier in the 15/15 sample. In the 15/15 specimen, the first stable "black dots" were observed at a dose around 0.15 dpa_{KP} whereas they are observed at a dose around 0.75 dpa_{KP} in the 15/25 specimen. Some unstable black dots were observed in the 15/25 sample between 0.3 and 0.8 dpa_{KP} (defects appeared and disappeared) but stable defect formation is only seen at higher doses. This suggests that an elimination mechanism occurs for those unstable defects.

During the experiment at the IVEM, defect-denuded zones were observed at 1 dpa_{KP} for both specimens. These zones were a few micrometers wide from the edge of the foil. This suggests that the free surfaces of the foil are strong sinks for point defects formed by irradiation preventing the formation of clusters in the thin regions of the sample.

The size of defects was measured from the micrographs using ImageJ. The defect size is equal to its diameter: if the defect is a "black dot", its size corresponds to its mean diameter; if the defect

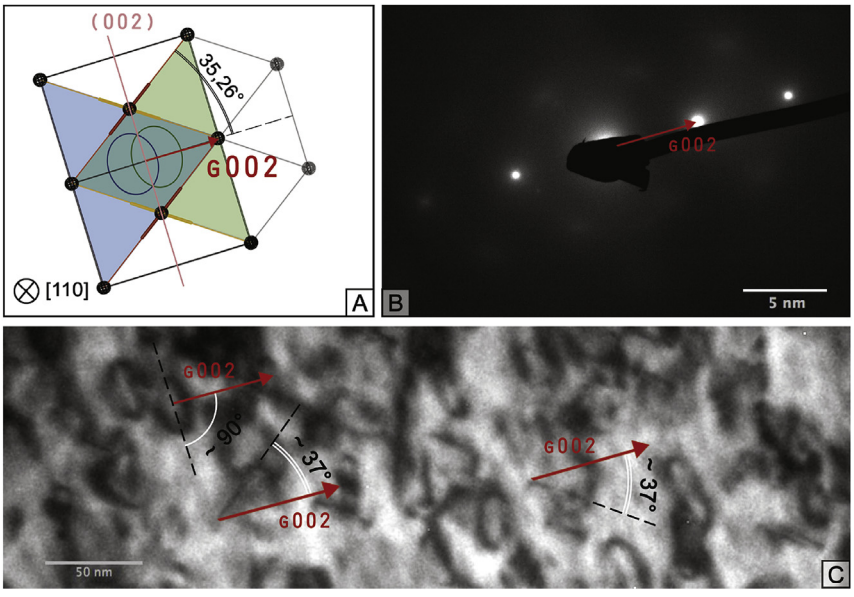

Fig. 8. {111} dislocation loops in 15Cr/15Ni–Ti specimen at 2,16 dpa_{KP}

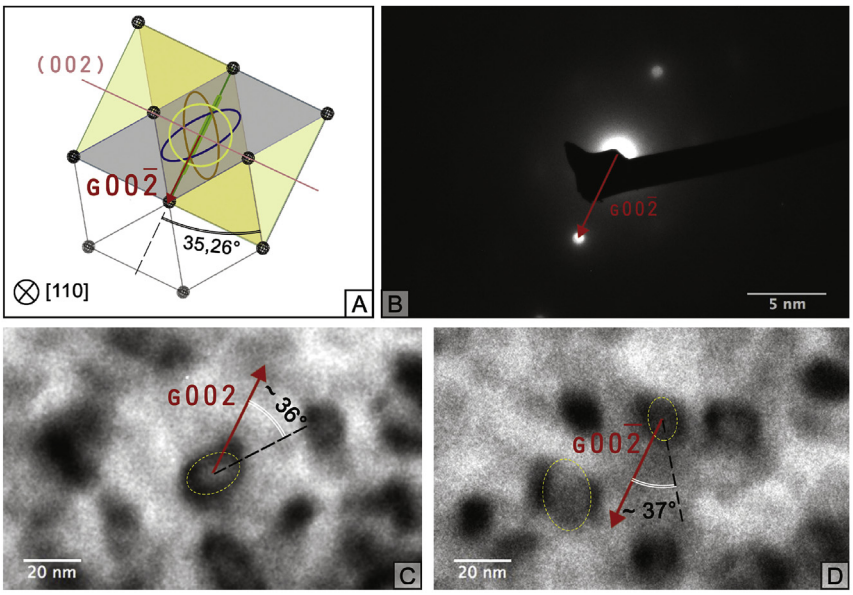

Fig. 9. {110} dislocation loops in 15Cr/25Ni–Ti specimen at 1,62 dpa_{KP}

is an elliptical loop, its size corresponds to the length of the major axis, which corresponds to the diameter of the circular loop in the {111} planes. If the defect is an edge-on loop, its size is the length of the visible segment. The number of defects measured at each dose was on the average higher than 500 for the 15/15 specimen and higher than 300 for the 15/25 specimen. The number of defects counted reached more than a thousand when the density of defects was very high. Statistical analysis of defect densities as function of dose is needed to show the results properly as the amount of data is substantial.

The mean loop size is plotted for both alloys in Fig. 11A and the statistical size distributions of dislocation loops are plotted in Fig. 11B, C and D. It is clear that loop growth is delayed in the 15Cr/25Ni–Ti alloy. At very low doses (< 2 dpa_{KP}), the distributions are concentrated because all the defects are small and have not yet coalesced. For both alloys, all loop distributions spread when the dose increases because dislocation loops increase and new loops appear continuously. Despite the spreading loop size distribution, it is fairly clear that the nucleation of defects occurs later in the 15Cr/25Ni–Ti alloy. The defect size evolution in the high Ni alloy is delayed by about 1 dpa relative to the low Ni alloy (see Fig. 11A), the two defect size distributions becoming similar at higher doses. In Fig. 11A, the growth rate of dislocation loops (as measured by the slope of the average loop size with dose) appears lower in the 15/15 alloy than in the 15/25 alloy. However, one must be careful in interpreting these results: for doses higher than 1 dpa_{KP} for the 15/15 alloy, and doses higher than 2 dpa_{KP} for the 15/25 alloy, many loops have already coalesced with other small loops. The number of loops measured between 1 and 2 dpa_{KP} is significant (between 400 and 1200, depending on the dose and the alloy), which means that many of the loops measured have already undergone coalescence. Consequently, the mean loop diameter (Fig. 11A) is strongly dependent on the coalescence process.

Although the average loop diameter gives a good idea of overall loop evolution, a complementary method is to follow the growth of a *single loop*. Performing the study in the IVEM allows to follow the growth of individual defects as a function of dose. The growth of dislocation loop diameter in individual loops was measured in the two model alloys for several defects (5 for the 15/15 and 5 for the 15/25), starting at approximately the same diameter (~15 nm) and which have not yet coalesced with other dislocation loops. The results of these measurements are plotted in Fig. 12.

The growth evolution of those individual defects shows similar slopes in both alloys: the estimated growth rate of loop diameter varies between 8.5 and 12.5 nm dpa_{KP}^{-1} for the 15/15 specimen and between 9.5 and 13.5 nm dpa_{KP}^{-1} for the 15/25 specimen. Note that the growth delay for the 15Cr/25Ni–Ti steel is approximately equal to 0.7 dpa_{KP}, which is close to the value found for the delay in nucleation dose. Note also that the calculation from Zinkle and co-workers indicate that faulted loops with a diameter in excess of 30 nm should be unstable with respect to unfaulting to perfect loops [28].

3.4. Density of dislocation loops

This section reports on the density of loops formed during irradiation. Since as mentioned above, the majority of loops were faulted, we report only on the density of faulted loops. This was partly confirmed by quantitative dislocation loop analysis performed on a 15/15 cold-worked sample irradiated up to 5 dpa (with the exact same conditions used to irradiate both 15/15 and 15/25 sample mentioned in IVEM experiment section). In that case, analysis shows that all loops are faulted. As the loops grow it is possible that some degree of loop unfaulting has taken place. It would be certainly be desirable to evaluate its extent by performing more detailed post irradiation analysis, which due to the damaged state of the samples is not possible to do.

In both alloys, the loop density was estimated as follows: for different areas (300×300 nm^2) of the irradiated region of interest, {111} elliptical loops were counted. Those defects are more easily visible than edge-on loops. Also, as stated above, the {111} loop density appears to be much higher than the {110} loop density. Consequently, only the {111} loop density is studied in this section. The probability that one loop is formed in one of the four {111} planes is the same. Two of those planes appear edge-on and the two others appear sloped (~ 35°) with respect to the observation axis. If the elliptical loops are the only defects counted, the total amount of {111} defects should be doubled to consider the edge-on defects.

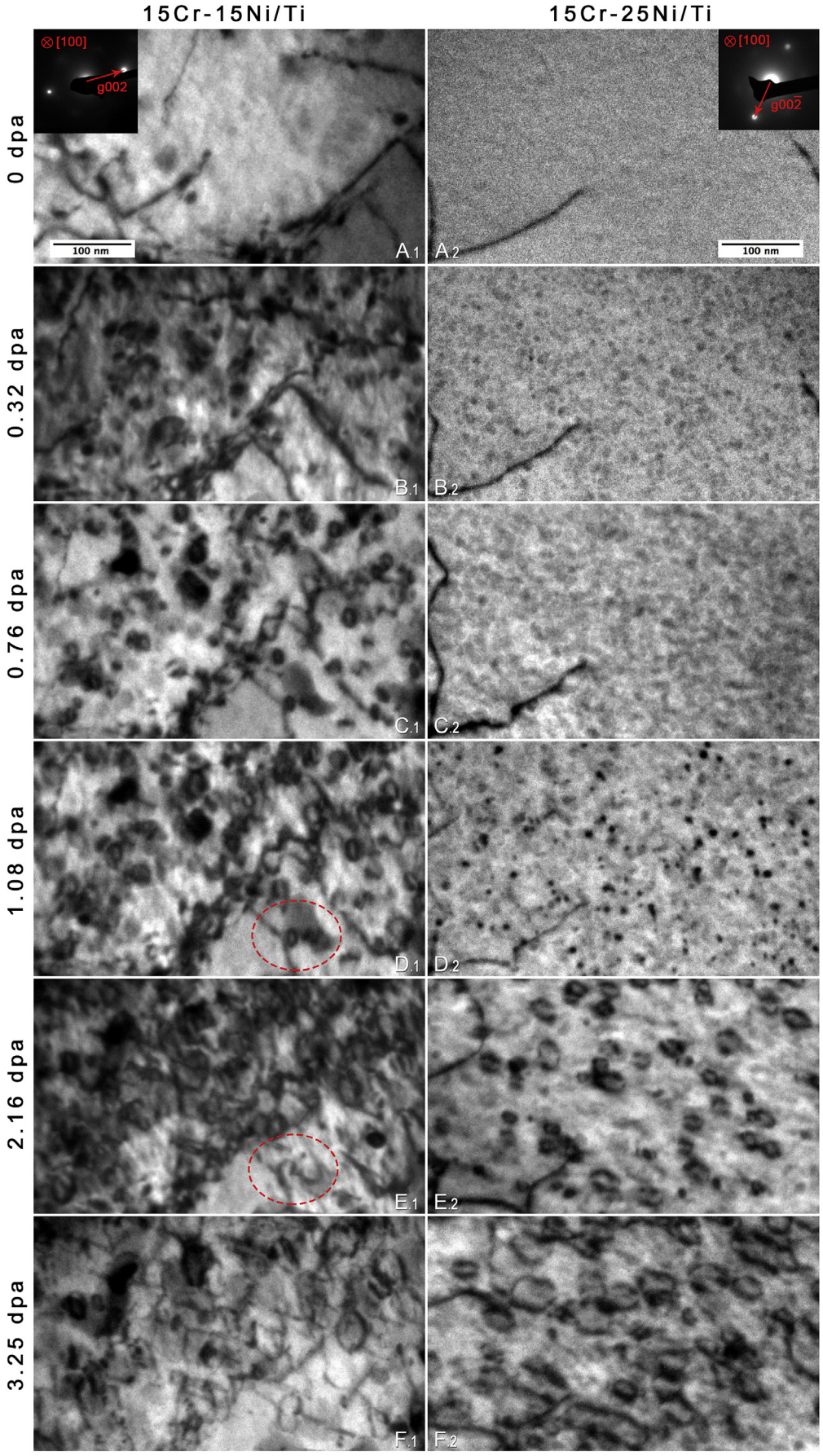

Fig. 10. Bright-field micrographs of 15Cr/15Ni–Ti (1) and 15Cr/25Ni–Ti (2) irradiated areas at five different doses: (A) 0 dpa_{KP}; (B) 0.32 dpa_{KP}; (C) 0.76 dpa_{KP}; (D) 1.08 dpa_{KP}; (E) 2.16 dpa_{KP}; (F) 3.25 dpa_{KP}.

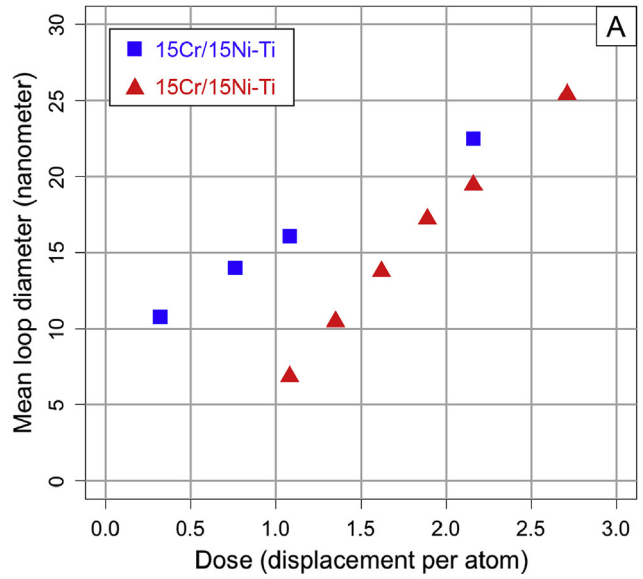

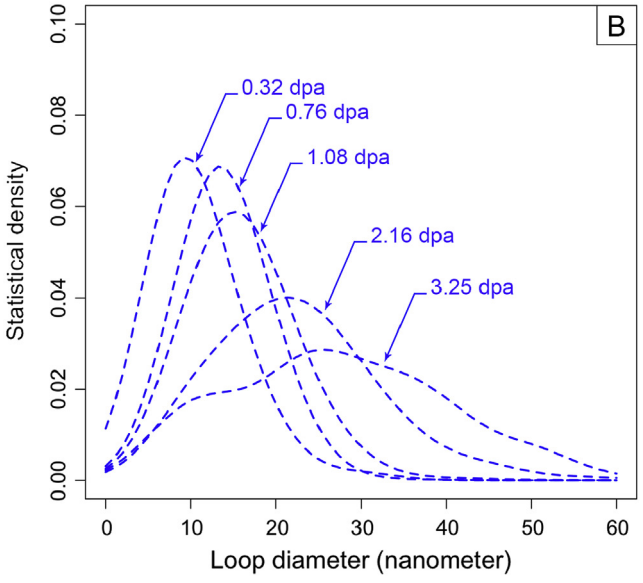

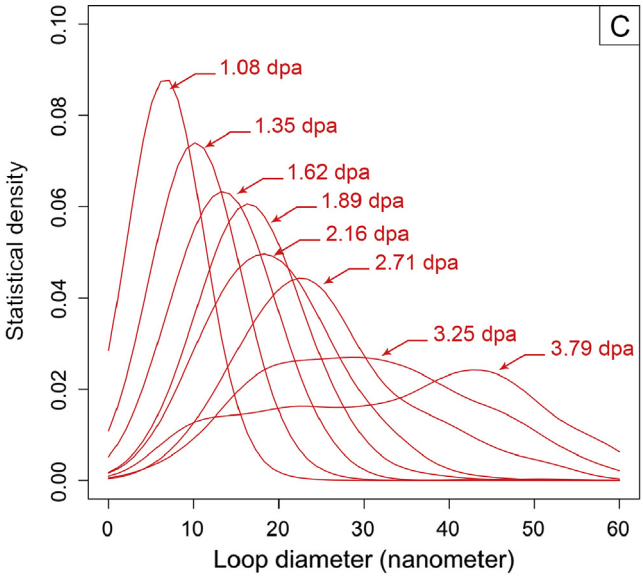

This amount of loops is divided by the total volume of the studied area, which depends on the sample thickness. For the 15/15 specimen, the thickness is equal to 150 ± 15 nm. The loop density for the 15/15 alloy is plotted as function of the dose in blue in Fig. 13. For the 15/25 specimen, which is thicker, it is more difficult to estimate the density because the sample thickness is not clearly known. In Fig. 13, the 15/25 loop densities, calculated with a thickness estimation of 200 nm and 300 nm, are plotted in red and purple respectively.

For both model alloys, the loop density increases quickly when the defect clusters are small "black dots" and then it diminishes because the defects coalesce with each other to form larger loops and eventually the dislocation network. In agreement with what was observed above, the loop nucleation appears at a higher dose (~0.75 dpa_{KP}) for the 15/25 alloy.

3.5. Cavities

Towards the end of the irradiation (20 dpa_{KP}), cavities were observed to form in both alloys (see Fig. 14). It was only possible to see those cavities in thin areas, where no dislocation loop was observed, using the overfocus/underfocus method. The average diameter of the cavities is below 5 nm. The density of those defects appears to be similar in the two alloys, and they appear homogenously dispersed in the grains. The fact that voids were only observed in the thin regions suggests that this is a thin foil effect. Nevertheless, this illustrates an excess of vacancies defects in the lattice, as discussed below.

4. Discussion

As discussed in the previous sections, the microstructure evolution under ion irradiation consisted of various stages: (i) appearance of visible clusters (black dot damage), (ii) defect clusters develop coffee bean contrast and grow, (iii) loops start coalescing with each other to form a dislocation network and (iv) at very high doses, small voids start to appear. The nature of the defects was similar in both alloys: the most common loop identified was one of the four variants of loops with a habit plane of {111} while a smaller percentage (1–5%) was constituted of {110}-type loops. Although the Burgers vector was not specifically determined, it is thought they are respectively $\vec{b} = (1/3)\langle 111\rangle$ and $\vec{b} = (1/2)\langle 110\rangle$[27].

Nucleation of the visible defect clusters was faster on the 15–15 (lower Ni content) sample than on the 15–25 (higher Ni content) sample, happening at 0.15 dpa_{KP} in the former and 0.75 dpa_{KP} in the latter. Once nucleated, the growth rate of the loops was similar (and rapid) in both alloys, indicating that loop formation is a nucleation-controlled process and that the effect of Ni is to retard the nucleation of the visible defects. At higher doses, the loop density starts to decrease, as loops start to coalesce.

Clearly the formation of visible loops (containing at least ~ 100 atoms) occurs gradually, requiring the formation of several classes of sub-visible clusters which absorb other mobile clusters or coalesce with other clusters to form the large visible clusters. To model this process properly, cluster dynamics should be used, in which rate equations are written for each of the defect size classes and rate constants derived for the transitions between different defect cluster sizes [30].

Fig. 11. Measures of dislocation loop size: (A) Mean loop diameter versus irradiation dose (dpa); (B) Statistical densities of loop sizes for the 15/15 model alloy; (C) Statistical densities of loop sizes for the 15/25 model alloy.

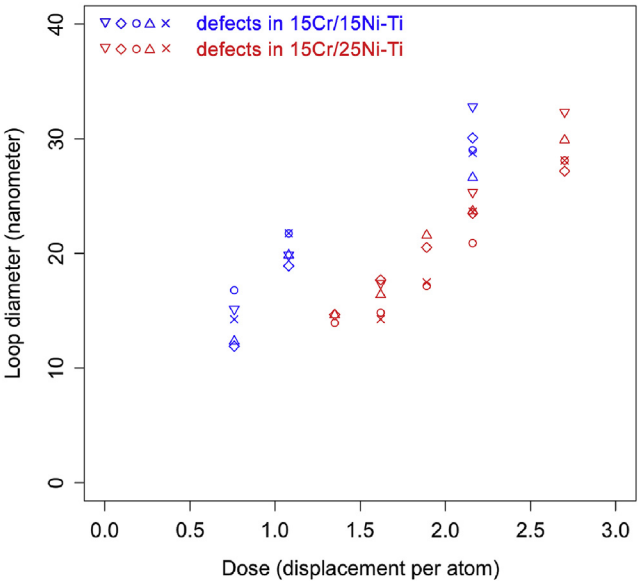

Fig. 12. Growth of several individual dislocation loops in 15Cr/15Ni–Ti and 15Cr/25Ni–Ti alloys. The measurement error is ± 2 nm.

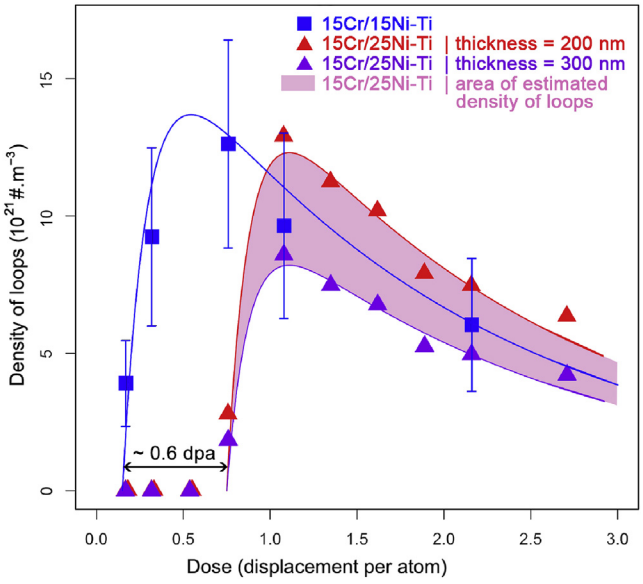

Fig. 13. Evolution of loop density in both alloys and fits according to equation (5).

This process (formation and annihilation of loops) can be roughly described using a semi-empirical model in two stages: the creation of loops by clustering of small defects and the coalescence of such loops. These two stages have different rate constants: formation rate k_1 and annihilation rate k_2.

$$\text{small defects} \xrightarrow[\text{clustering}]{k_1} \text{dislocation loops} \tag{2}$$

$$\text{dislocation loops} \xrightarrow[\text{coalescence}]{k_2} \text{dislocation lines} \tag{3}$$

The integration of the kinetic equation (4) gives the evolution of loop density (5):

$$\begin{cases} \dfrac{\mathrm{d}\,\rho_{\text{small defects}}}{\mathrm{d}\,d} = -k_1 \cdot \rho_{\text{small defects}} \\ \dfrac{\mathrm{d}\,\rho_{\text{disl.loops}}}{\mathrm{d}\,d} = k_1 \cdot \rho_{\text{small defects}} - k_2 \cdot \rho_{\text{disl.loops}} \\ \dfrac{\mathrm{d}\,\rho_{\text{disl.lines}}}{\mathrm{d}\,d} = k_2 \cdot \rho_{\text{disl.loops}} \end{cases} \tag{4}$$

$$\forall d > d_0, \rho_{\text{disl.loops}} = A_0 \cdot k_1 \cdot \frac{e^{-k_1 \cdot (d-d_0)} - e^{-k_2 \cdot (d-d_0)}}{k_2 - k_1} \tag{5}$$

where:

- $\rho_{\text{small defects}}$: small defect density [# μm^{-3}]
- $\rho_{\text{disl. loops}}$: disl. loop density [# μm^{-3}]
- $\rho_{\text{disl. lines}}$: disl. line density
- d: dose [dpa_{KP}]
- d_0 : nucleation dose [dpa_{KP}]
- A_0 : fitting constant [# μm^{-3}]

Although this simple equation does not reflect the physics behind the phenomena (ignore homogeneous nucleation, assumes all small cluster and loop sizes react at the same rates, etc.), it fits the density data well (they represent the solid lines in Fig. 13). For both alloys, the rate constants are similar and their values are $k_1 \simeq 7\ s^{-1}$ and $k_2 \simeq 0.55\ s^{-1}$. These constants were obtained by fitting the data sets on Fig. 13 with equation (5). This suggests that the growth rate is the same in both model materials, which was previously illustrated by the analysis of individual defect growth. The difference between the nucleation doses of 15Cr/15Ni–Ti and 15Cr/25Ni–Ti (d_0 in the model) is equal to 0.6 dpa_{KP}, which is close to the values observed previously.

It was not determined from our study whether the loops formed were interstitial or vacancy in nature. It is clear that only a small percentage of defects participates in loop formation. A rough calculation of the ratio of the number of atoms present in visible loops to the total number of displaced atoms, at 1 dpa_{KP}, gives a value of about 0.02%. That is, only 2×10^{-4} atoms are not either absorbed in sinks, recombining or accumulating in the lattice as sub-visible defects. It is also noteworthy that a defect-free zone is observed near the specimen edge, indicating that some defects are lost to the surface, suggesting that the sample surface is an important sink.

Because the interstitial mobility is higher than that of the vacancies [31], one possible mechanism for loop formation is that interstitials migrate to the surface and are absorbed, leaving an excess of vacancies which then cluster and collapse into dislocation loops. In this case the effect of nickel would be to retard the nucleation of vacancy loops, either by segregating to the loop and increasing the stacking fault energy or by pinning the defects that would normally migrate to the loops in the matrix. However once the loops are nucleated, the growth rate in both alloys is similar, suggesting that the migration of defect clusters to the loops is not affected by Ni content.

The other possibility is that these are interstitial loops. Interstitials have a stronger elastic interaction with defect clusters [32], which can result in a selection of interstitials to arrive at the dislocation loops. In this case the vacancies would be preferentially accumulating in the lattice as sub-visible defect clusters [26]. have identified dislocation loops formed in austenitic steels under neutron irradiation as being interstitial in nature. The fact that cavities appear at high doses would support this hypothesis, if one assumes that at high doses such sub-visible excess vacancy defects would cluster and grow.

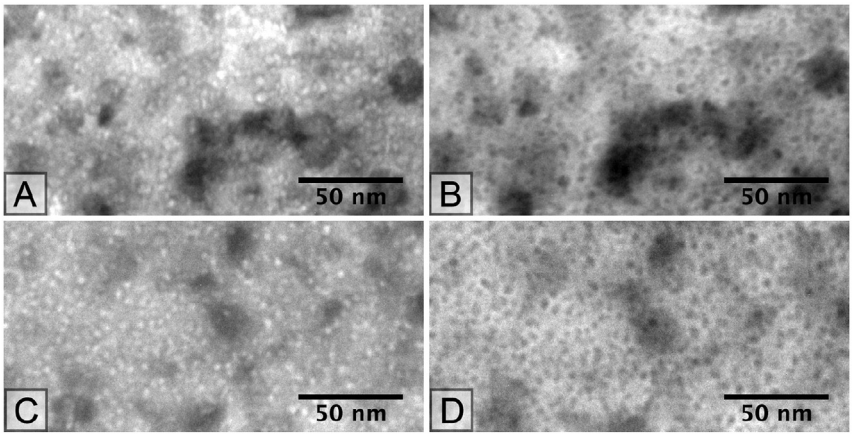

Fig. 14. Cavities at 20 dpa_{KP}. (A) 15Cr/15Ni–Ti underfocused; (B) 15Cr/15Ni–Ti overfocused; (C) 15Cr/25Ni–Ti underfocused; (D) 15Cr/25Ni–Ti overfocused.

5. Conclusions

The microstructure evolution under 1Me V Kr ion irradiation of 15Cr/15Ni and 15Cr/25Ni austenitic steels, both stabilized with titanium and aged 24 h at 800° C after a solution annealing, was investigated in-situ. The observations of the irradiated microstructures lead to the following conclusions:

1. Dislocation loops evolve into three stages: nucleation, growth and coalescence.
2. The majority of dislocation loops are found in {111} planes. A smaller number of loops are located in {110} planes.
3. Nickel in solid solution increases the incubation dose of small defect clusters.
4. Cavities, with a diameter lower than 5 nm, were observed in thin areas of both model alloys at 20 dpa_{KP}.

Acknowledgments

The electron microscopy with in situ ion irradiation was accomplished at Argonne National Laboratory at the IVEM-Tandem Facility, a U.S. Department of Energy Facility funded by the DOE Office of Nuclear Energy, operated under Contract No. DE-AC02-06CH11357 by UChicago Argonne, LLC.

The authors would like to thank warmly E. Ryan and P. Baldo from Argonne National Laboratory for assistance with the in-situ TEM experiments, J. Gray from Penn State University for assistance with the post-irradiation thickness measurements and C. Ulmer from Penn State University for his help with the preparation of samples.

Nomenclature

x	damage value computed with SRIM [$dpa_{KP}ion^{-1}$ cm^{-1}]
Φ	ion flux [ions cm^{-2} s^{-1}]
t	irradiation time [s]
$\mathscr{M}$	sample molar mass [g mol^{-1}]
ρ	volumetric mass [g cm^{-3}]
$\mathcal{N}_{\mathcal{A}}$	Avogadro number [mol^{-1}]
$\rho_{\text{small defects}}$	small defect density [# μm^{-3}]
$\rho_{\text{disl. loops}}$	disl. loop density [# μm^{-3}]
$\rho_{\text{disl. lines}}$	disl. line density
d	dose [dpa_{KP}]
d_0	nucleation dose [dpa_{KP}]
k_i	rate constant [s^{-1}]

References

[1] B. Rouxel, C. Bisor, Y. de Carlan, A. Courcelle, A. Legris, Influence of the austenitic stainless steel microstructure on the void swelling under ion irradiation, in: Proc. Int. Congress on Advances in Nuclear Power Plants (ICAPP '15), Nice, France, May 03-06, 2015, Paper 15481, American Nuclear Society (2015) (CD-ROM), 2015.
[2] C. Cawthorne, E.J. Fulton, Voids in irradiated stainless steel, Nature 216 (1967) 575–576.
[3] J.L. Straalsund, R.W. Powell, An overview of neutron irradiation effects in LMFBR materials, J. Nucl. Mater. 108–109 (1993) 166–186.
[4] L.K. Mansur, Theory and experimental background on dimensional changes in irradiated alloys, J. Nucl. Mater. 216 (1994) 97–123.
[5] V.S. Neustroev, F.A. Garner, Severe embrittlement of neutron irradiated austenitic steels arising from high void swelling, J. Nucl. Mater. 386 (2009) 157160.
[6] E. Wakai, N. Hashimoto, J.P. Robertson, T. Sawai, A. Hishinuma, Swelling of cold-worked austenitic stainless steels irradiated in HFIR under spectrally tailored conditions, J. Nucl. Mater. 307–311 (2002) 352–356.
[7] S. Hamada, M. Suzuki, P.J. Maziasz, A. Hishinuma, Microstructural evolution in austenitic stainless steels irradiated to 57 dpa in HFIR, J. Nucl. Mater. 179–181 (1991) 515–518.
[8] M. Le Flem, P. Gavoille, Y. de Carlan, C. Bisor, J.L. Séran, Advanced steel claddings for SFRS: feedback and challenges, GETMAT (2013). CEA Saclay, September 2013.
[9] E. Lee, L.K. Mansur, Fe-15Ni-13Cr austenitic stainless steels for fission and fusion reactor applications. III. Phase stability during heavy ion irradiation, J. Nucl. Mater. 278 (2000) 20–29.
[10] P.J. Maziasz, Overview of microstructural evolution in neutron-irradiated austenitic stainless steels, J. Nucl. Mater. 205 (2006) 118–145.
[11] I.M. Neklyudov, V.N. Voyevodin, Radiation swelling of modified austenitic steels, Russ. Phys. J. 51 (4) (2006) 400–413.
[12] V.N. Voyevodin, I.M. Neklyudov, V.V. Bryk, O.V. Borodin, Microstructural evolution and radiation stability of steels and alloys, J. Nucl. Mater. 271–272 (1999) 290–295.
[13] B. Raj, M. Vijayalakshmi, Radiation damage of structural materials for fast reactor fuel assembly, ICTP/IAEA Sch. (2009). Trieste (*Italy*), November, 9-20, 2009.
[14] M. Terada, M. Saiki, I. Costa, A.F. Padilha, Microstructure and intergranular corrosion of the austenitic stainless steel 1.4970, J. Nucl. Mater. 358 (2006) 40–46.
[15] A.F. Padilha, G. Schanz, K. Anderko, Ausscheidungsverhalten des titan-stabilisierten austenitischen stahls 15% Q-15% Ni-1% Mo-Ti-B (din-werkstoff-NR. 1.4970), J. Nucl. Mater. 150 (1982) 77–92.
[16] T. Muroga, F.A. Garner, S. Ohnuki, Microstructural investigation of swelling dependence on nickel content in fast neutron-irradiated Fe-Cr-Ni austenitic ternaries, J. Nucl. Mater. 179–181 (1991) 546–549.
[17] O.V. Borodin, V.V. Bryk, A.S. Kalchenko, V.V. Melnichenko, V.N. Voyevodin, F.A. Garner, Synergistic effects of helium and hydrogen on self-ion-induced swelling of austenitic 18Cr10NiTi stainless steel, J. Nucl. Mater. 442 (2013) S817–S820.
[18] F.A. Garner, Recent insights on the swelling and creep of irradiated austenitic alloys, J. Nucl. Mater. 122–123 (1984) 459–471.
[19] C. David, B.K. Panigrahi, S. Balaji, A.K. Balamurugan, K.G.M. Nair, G. Amarendra, C.S. Sundar, B. Raj, A study of the effect of titanium on the void swelling behavior of D9 steels by ion beam simulation, J. Nucl. Mater. 383 (2008) 132–136.
[20] R.F. Egerton, Electron Energy-loss Spectroscopy in the Electron Microscope, second ed., Plenum Press, New-York, 1996.

[21] R.F. Egerton, S.C. Cheng, Measurement of local thickness by electron energy-loss spectroscopy, Ultramicroscopy 21 (1987) 231–244.
[22] T. Malis, S.C. Cheng, R.F. Egerton, EELS log-ratio technique for specimen-thickness measurement in the TEM, J. Electron Microsc. Tech. 8 (1988) 193–200.
[23] K. Iakoubovskii, K. Mitsuishi, Y. Nakayama, K. Furuya, Thickness measurements with electron energy loss spectroscopy, Microsc. Res. Tech. 71 (2008) 626–631.
[24] R.E. Stoller, M.B. Toloczko, G.S. Was, A.G. Certain, S. Dwaraknath, F.A. Garner, On the use of SRIM for computing radiation damage exposure, Nucl. Instrum. Methods Phys. Res. B 310 (2013) 75–80.
[25] C. Topbasi, A.T. Motta, M.A. Kirk, DIn situ study of heavy ion induced radiation damage in NF616 (P92) alloy, J. Nucl. Mater. 425 (2012) 48–253.
[26] S.J. Zinkle, P.J. Maziasz, R.E. Stoller, Dose dependence of the microstructural evolution in neutron-irradiated austenitic stainless steel, J. Nucl. Mater. 206 (1993) 266–286.
[27] YuN. Osetsky, D.J. Bacon, A. Serra, B.N. Singh, S.I. Golubov, Stability and mobility of defect clusters and dislocation loops in metals, J. Nucl. Mater. 276 (2000) 65–77.
[28] S.J. Zinkle, L.E. Seitzman, W.G. Wolfer, I. Energy calculations for pure metals, Philos. Mag. A 55 (1) (1987) 111–125.
[29] M.P. Wand, M.C. Jones, Kernel Smoothing, CRC Press, Boca Raton, Florida, 1995.
[30] T.R. Allen, D. Kaoumi, J.P. Wharry, Z. Jiao, C. Topbasi, A. Kohnert, L. Barnard, A. Certain, K.G. Field, G.S. Was, Characterization of microstructure and property evolution in advanced cladding and duct: materials exposed to high dose and elevated temperature, J. Mater. Res. 30 (2015) 1246–1274.
[31] Mansur, L.K. (1987), Kinetics of nonhomogeneous processes, ed. G.R. Freeman (Wiley, New York, 1987) pp. 377-463; L.K. Mansur, Nucl. Technol. 40 (1978) 5.
[32] A.D. Brailsford, R. Bullough, The rate theory of swelling due to void growth in irradiated metals, J. Nucl. Mater. 44 (1972) 121–135.